

# Snapshot projection optical tomography

Yongjin Sung  
College of Engineering & Applied Science  
University of Wisconsin  
Milwaukee, WI 53211  
ysung4@uwm.edu

June 12, 2019

## Abstract

We present a new plenoptic microscopy configuration consisting of an objective lens and a micro-lens array (MLA), which is used as a tube lens. The new system that we named as snapshot projection optical tomography (SPOT) can directly record the projection images corresponding with different viewing angles, and it contrasts with existing plenoptic imaging, which uses an MLA as a Shack-Hartmann sensor. For a theoretical analysis, we extended a 3-D forward imaging model for high-NA telecentric system. We also acquired the image of a  $6\text{-}\mu\text{m}$  fluorescence bead, which clearly showed the optical-sectioning capability of SPOT.

## 1 Introduction

Fluorescence microscopy allows imaging the distribution of biomolecules within a cell, tissue or animal, and it has become an essential tool in biomedical researches and clinical practices[1]. A variety of new molecular probes and gene manipulation techniques are adding more functionalities to fluorescence microscopy. For recording the 3-D distribution of fluorophores, whether they are reactive dyes, quantum dots or fluorescent proteins, three strategies are typically used: scanning a focused beam[2] or a light sheet across the 3-D volume[3]; moving the sample across the focal plane to acquire images at different depths[4]; or rotating the sample to acquire different projection images[5] as in X-ray computed tomography (CT)[6]. These are distinguished from 3-D surface imaging[7] or digital holography[8], which record only limited information about the sample. To acquire the 3-D volume with complex internal structure, several hundreds of 2-D images should be recorded, which may take a fraction of a second even with recent fast cameras. Because samples can move or change their shape during the data acquisition, the scanning-based techniques are not appropriate for high-speed 3-D imaging. Snapshot volumetric imaging has been

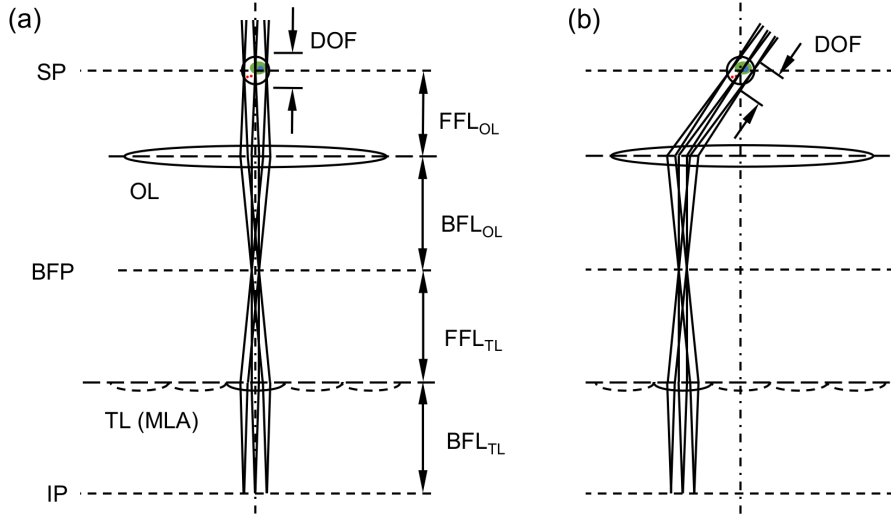


Figure 1: Snapshot projection optical tomography. SP: sample plane; BFP: back focal plane; IP: image plane; objective lens (OL); tube lens (TL); FFL: front focal length; BFL: back focal length; and DOF: depth of field. The dash-dot line represents the optical axis of OL. Each lenslet in the MLA records a projection image corresponding with a different viewing angle.

developed to overcome this limitation[9], in which different depth layers, typically less than 10 layers, are remapped to different areas of the camera using a volume hologram[10], a distorted grating[11], or a liquid-crystal spatial light modulator[12]. Simultaneous imaging of 49 layers at a coarse axial resolution of  $38 \mu\text{m}$  has been recently demonstrated using a distorted Dammann grating[13]. Most notably, light-field microscopy (LFM)[14] records a 4-D light field (i.e., 2-D spatial and 2-D angular distribution of intensity among light rays), from which the projection images corresponding with different viewing angles can be synthesized and the depth information extracted. The original LFM, which was derived from plenoptic camera[15], is known to suffer from non-uniform spatial resolution across depth[16]; however, it has been demonstrated that the problem can be greatly mitigated using wavefront coding[17], i.e., placing phase masks in the beam path. LFM has been successfully adopted to record neuronal activities in the brain tissues of *C. elegans* and small zebrafish[18, 19]. Here we present a new plenoptic microscopy configuration, which we named as snapshot projection optical tomography (SPOT). SPOT directly records all the projection images corresponding with different viewing angles, and thus allows optical tomography in a single snapshot.

In SPOT, a microlens array (MLA) is used as a tube lens (TL) and it is arranged with the objective lens (OL) in a 4-f telecentric configuration. The 4-f configuration means that the sample is placed at the front focal plane of OL; that

the distance between the two lenses is the same as the sum of their focal lengths ( $BFL_{OL}$  and  $FFL_{TL}$ ); and that the camera is placed at the back focal plane of TL. This configuration is in sharp contrast with other plenoptic imaging[20] including LFM, in which an MLA is used as a Shack-Hartmann sensor and typically placed at the image plane. Fig.1(a) shows the lens arrangement in the proposed system together with the beam paths through the lenslet centered at the optical axis. The depth of field (DOF) of an optical microscope is inversely proportional to the square of numerical aperture (NA). Of note, when a 2-D array of lenslets is used to capture  $m \times m$  projection images, the effective NA for each projection image is reduced to by  $NA/m$ . Due to the reduced effective NA, or increased DOF, the emitters on a line parallel with the optical axis generate focused beams at the image plane through the on-axis lenslet. In other words, the image recorded by the on-axis lenslet can be considered as the projection of the fluorophore distribution along the optical axis direction. Fig. 1(b) shows the beam paths from the sample to the image plane through an off-axis lenslet. Here the emitters on a tilted line with respect to the optical axis generate focused beams at the image plane through the lenslet. In a 4-f configuration, the tilt angle is determined by the lateral offset of lenslet center from the optical axis. Thus, using an MLA as a tube lens, we can record the projection images of a 3-D fluorophore distribution, which correspond with different viewing angles, in a single snapshot. Applying a tomographic reconstruction algorithm such as the inverse Radon transform, we can obtain the 3-D fluorophore distribution in the sample.

## 2 Theory

A high-NA telecentric system, which consists of two lenses sharing the same optical axis, has been studied by Sheppard and Gu[21]. SPOT consists of a high-NA objective lens (OL) and an array of lenslets, each of which is in the same 4-f configuration with OL but has a different offset from the optical axis of OL. Fig.2 shows the imaging geometry and the coordinate systems adopted in the analysis. The focal lengths of OL and MLA are  $f_1$  and  $f_2$ , respectively. Consider that a point source of amplitude  $U_1$  is placed at  $(x_1, y_1, z_1)$  and radiates isotropically. The amplitude in the pupil plane with the coordinates  $\xi$  and  $\eta$  can be written as

$$U(\xi, \eta) = -\frac{ia_1^{-1}(\xi, \eta)}{\lambda f_1} U_1 \exp \left\{ \frac{ik}{f_1} (x_1 \xi + y_1 \eta + z_1 \zeta) \right\}, \quad (1)$$

where  $\zeta = [f_1^2 - (\xi^2 + \eta^2)]^{1/2}$ . The apodization factor  $a_1(\xi, \eta)$  is  $[1 - (\xi^2 + \eta^2)/f_1^2]^{1/4}$  for the sine condition and 1 for the Herschel condition.

Suppose that we project the lenslet aperture centered at  $(\xi, \eta) = (\bar{\xi}_m, \bar{\eta}_m)$  onto the pupil plane. We also define a local coordinate system  $(\xi', \eta')$  with the origin at the lenslet center, as shown in Fig. 2. Of note,  $(\xi, \eta, \zeta)$  in Eq. 1 represents a hemispherical surface, which can be approximated by piecewise-planar surfaces (e.g., the surface shown as the thick line in Fig.2). For a lenslet centered at

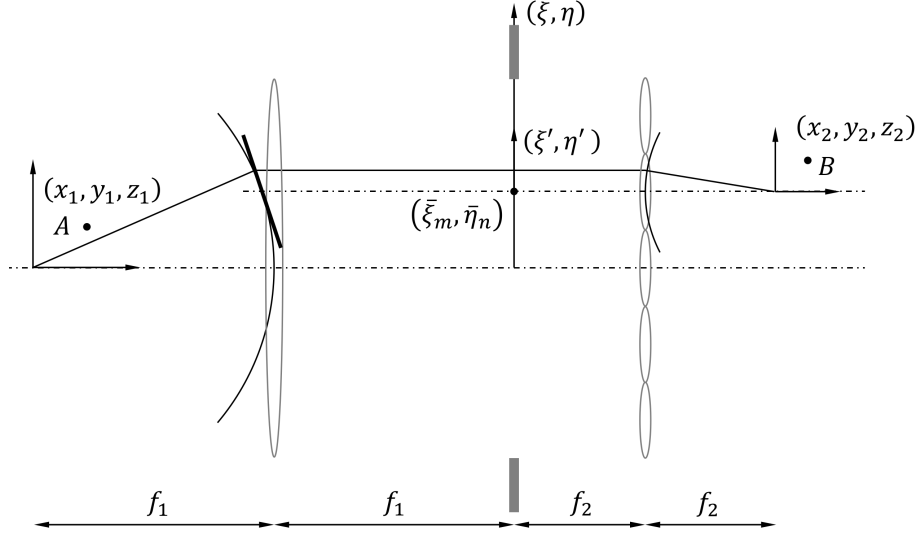


Figure 2: Schematic diagram of the imaging geometry.

$(\xi, \eta) = (\bar{\xi}_m, \bar{\eta}_n)$ ,  $\zeta \approx c(f_1^2 - \bar{\xi}_m \xi - \bar{\eta}_n \eta)$ , where  $c = [f_1^2 - (\bar{\xi}_m^2 + \bar{\eta}_n^2)]^{-1/2}$ . This approximation is valid as far as the NA of lenslets is small, although the NA of OL can be very large. Then the amplitude in the pupil plane due to a point source at  $(x_1, y_1, z_1)$  in the sample space can be written as

$$U'(\xi', \eta') = -\frac{ia_1^{-1}(\xi' + \bar{\xi}_m, \eta' + \bar{\eta}_n)}{\lambda f_1} U_1 \exp(ik f_1 z_1 c) \times \exp\left\{\frac{ik}{f_1} [(x_1 - \Delta x_1)(\xi' + \bar{\xi}_m) + (y_1 - \Delta y_1)(\eta' + \bar{\eta}_n)]\right\}, \quad (2)$$

where  $\Delta x_1 = z_1 \tan(\alpha_m)$  and  $\Delta y_1 = z_1 \tan(\beta_n)$ .  $\alpha_m$  and  $\beta_n$  are the angles determined by the focal length  $f_1$  and the offset  $\bar{\xi}_m$  and  $\bar{\eta}_n$  of the lenslet center along the  $\xi$  and  $\eta$  direction. As we will show, these angles determine the viewing direction, along which the fluorescence signal is added.

$$\tan(\alpha_m) = \frac{\bar{\xi}_m}{[f_1^2 - (\bar{\xi}_m^2 + \bar{\eta}_n^2)]^{1/2}}, \quad \tan(\beta_n) = \frac{\bar{\eta}_n}{[f_1^2 - (\bar{\xi}_m^2 + \bar{\eta}_n^2)]^{1/2}}. \quad (3)$$

The amplitude at B can be written in terms of the amplitude  $U'(\xi', \eta')$  in the pupil plane as

$$U_2(x_2, y_2) = -\frac{i}{\lambda f_2} \iint U'(\xi', \eta') P(\xi', \eta') a_2(\xi', \eta') \times \exp\left\{\frac{ik}{f_2} (x_2 \xi' + y_2 \eta')\right\} d\xi' d\eta', \quad (4)$$

where  $P(\xi', \eta')$  is the pupil function, which includes optical aberration. The apodization factor  $a_2(\xi', \eta')$  is  $\left[1 - (\xi'^2 + \eta'^2)/f_2^2\right]^{1/4}$  for the sine condition and 1 for the Herschel condition. Substituting Eq. 2 and excluding a phase factor, Eq. 4 can be written as

$$U_2(x_2, y_2) = -\frac{U_1}{\lambda^2 f_1 f_2} \Psi\left(-\frac{x_2 + x_{2s}}{\lambda f_2}, -\frac{y_2 + y_{2s}}{\lambda f_2}\right), \quad (5)$$

where  $M = f_2/f_1$  is the magnification,  $x_{2s} = M(x_1 - \Delta x_1)$ ,  $y_{2s} = M(y_1 - \Delta y_1)$ , and

$$\begin{aligned} \Psi(u, v) &= \mathcal{F} \left\{ \frac{a_2(\xi', \eta')}{a_1(\xi' + \bar{\xi}_m, \eta' + \bar{\eta}_n)} P(\xi', \eta') \right\} \\ &= \iint_{-\infty}^{\infty} \frac{a_2(\xi', \eta') P(\xi', \eta')}{a_1(\xi' + \bar{\xi}_m, \eta' + \bar{\eta}_n)} \exp\{-i2\pi(u\xi' + v\eta')\} d\xi' d\eta'. \quad (6) \end{aligned}$$

The aberration-free pupil function for a rectangular lenslet can be expressed as  $P(\xi', \eta') = \text{rect}(\xi'/p)\text{rect}(\eta'/p)$ , where  $p$  is the pitch of MLA, and  $\text{rect}(x) = 1$  (for  $|x| < 1/2$ );  $1/2$  (for  $|x| = 1/2$ ); and 0 otherwise. The 2-D Fourier transform of  $P(\xi', \eta')$  is  $\tilde{P}(u, v) = p^2 \text{sinc}(pu)\text{sinc}(pv)$ , where  $\text{sinc}(x) = \sin(\pi x)/(\pi x)$ . Then the amplitude at the image plane, Eq. 5, can be simply expressed as

$$U_2(x_2, y_2) = -\frac{U_1 p^2}{\lambda^2 f_1 f_2} \text{sinc}\left(\frac{x_2 + x_{2s}}{\lambda f_2/p}\right) \text{sinc}\left(\frac{y_2 + y_{2s}}{\lambda f_2/p}\right). \quad (7)$$

Finally the intensity at the image plane, or the 2-D point spread function (PSF), is given by

$$I_2(x_2, y_2) \propto \text{sinc}^2\left(\frac{x_2 + x_{2s}}{\lambda f_2/p}\right) \text{sinc}^2\left(\frac{y_2 + y_{2s}}{\lambda f_2/p}\right). \quad (8)$$

Eq. (8) shows that the image of an out-of-focus emitter is centered at  $(-x_{2s}, -y_{2s})$ . Fig. 3 shows how  $x_{2s}$  and  $y_{2s}$  are related to the imaging parameters and the sample's location. The hemispherical surface represents a diverging wavefront from an on-axis, in-focus point source and has the radius of  $f_1$ , the focal length of objective lens. Let us project the lenslet center onto the hemispherical surface then draw a vector from the intersection point to the center of hemisphere. The direction of the vector represents the viewing angle of MLA.  $\alpha_m$  and  $\beta_n$  are the angles that the projections of the vector onto  $\xi\zeta$  and  $\eta\zeta$  planes, respectively, make with the  $\zeta$  axis. Fig. 3(b) shows an out-of-focus point source at  $(x_1, y_1, z_1)$  and the vector we defined in Fig. 3(a). Projecting the point source along the vector direction, in the  $z = 0$  plane, the intersection point is shifted from  $(x_1, y_1)$ . The offset along the  $x$  and  $y$  direction correspond to  $\Delta x_1$  and  $\Delta y_1$ , respectively. The 2-D PSF has its first minima at the distance of  $\lambda f_2/p$ , i.e.,  $\lambda/(2\text{NA}_{\text{MLA}})$ , from the center, where  $\text{NA}_{\text{MLA}}$  is the numerical aperture of micro-lens array. This corresponds to the full width at half maximum of  $0.443\lambda/\text{NA}_{\text{MLA}}$ . Because a sample consisting of a large number of fluorophores

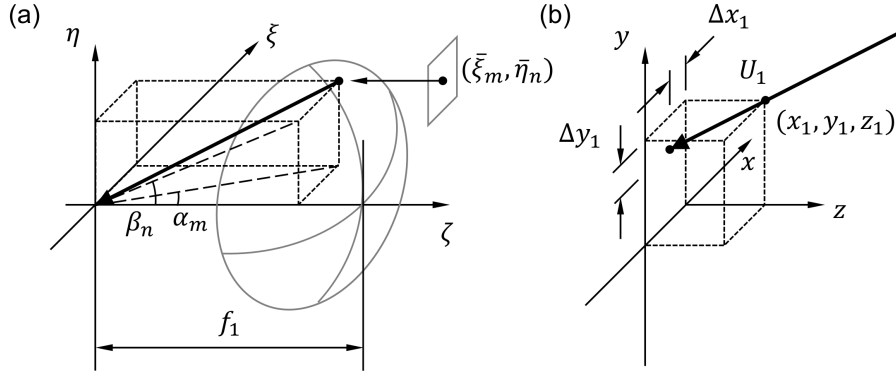


Figure 3: Geometrical interpretation of the projection operation performed by an off-axis lenslet in SPOT. (a) The projection direction is determined by the offset of lenslet center and the focal length of objective lens. (b) An out-of-focus point is projected onto the  $z = 0$  plane along the projection direction determined in (a).

can be represented by a superposition of point emitters, its image can be calculated by adding up the intensity distributions given by Eq. (8) for different  $(x_1, y_1, z_1)$  values.

### 3 Experiment

We modified an inverted fluorescence microscope (Zeiss Axiostar) and built a prototype SPOT system. Fig.4(a) shows the schematic diagram with the example excitation and the emission beam paths separately shown as solid and dotted lines, respectively. The excitation beam was collimated by a beam expander, reflected off the dichroic mirror in the fluorescence filter cube and introduced into the sample plane, as is done in a typical epi-fluorescence microscope. The dotted lines are emission beam paths for an on-axis point emitter at the sample plane. The fluorescent light emitted from the sample was captured by OL (Olympus, UPlanFl 100X, 1.3 NA), and, after the TL, recorded by the camera (Allied Vision, Stingray F-504C) with  $2452 \times 2056$  pixels and  $3.45 \mu\text{m}$  pitch. Once the projection images are acquired, we can apply a tomographic reconstruction algorithm such as the inverse Radon transform[6] to obtain the 3-D fluorophore distribution in the sample volume. The inverse Radon transform, originally developed for X-ray CT, can be applied to optical imaging when the optical rays are recorded using a low (effective) NA optical system [5].

We imaged a  $6\text{-}\mu\text{m}$  polystyrene bead (Fisher Scientific, F14806), whose outermost layer is stained with green/orange/dark-red fluorescent dye, using a filter set for green fluorescent proteins (GFP). For this experiment, we adopted an MLA (Edmund, 64-483) with the focal length of 46.7 mm and the pitch of 500

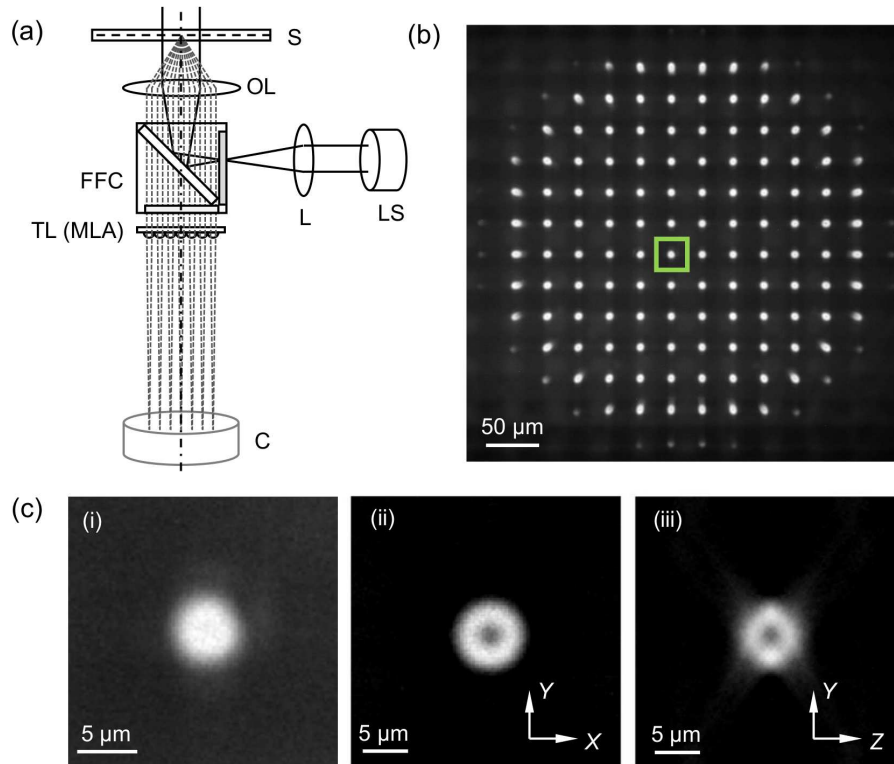


Figure 4: Snapshot 3-D fluorescence imaging (a) Schematic diagram of an exemplary system showing the excitation beam path (solid lines) and emission beam paths (dotted lines) from an on-axis point to the camera. LS: light source; BE: beam expander; S: sample; L: lens; OL: objective lens; TL: tube lens; MLA: micro-lens array; FFC: fluorescence filter cube; and C: camera. (b-c) Snapshot 3-D imaging of a  $6\text{-}\mu\text{m}$  polystyrene bead with the outermost layer stained with fluorescent dye: example raw image (b) with a zoomed-in view of the rectangular box (c,i). (c) Horizontal (ii) and vertical (iii) cross-section of the bead after tomographic reconstruction.

$\mu\text{m}$ . Due to the small focal length of MLA, we inserted two lenses between OL and MLA. All the lenses were in 4-f configuration. We further magnified the image formed by MLA by 1.5 times to fully utilize the camera pixels. For these choices of parameters, the field of view was  $29 \mu\text{m}$ , and the pixel resolution was  $0.2 \mu\text{m}$ . For the center wavelength (505 nm) of GFP emission band and  $\text{NA}_{\text{MLA}}$  of 0.18, the theoretical resolution was  $1.2 \mu\text{m}$ . The raw image shown in Fig.4(b) contains a multitude of projection images, each of which corresponds with a specific viewing angle. Applying the inverse Radon transform to the projection images, we reconstructed the 3-D fluorescence image of the bead. Fig.4(c) compares a projection image (i) with a horizontal (ii) and a vertical (iii) cross-section of the reconstructed bead. The stained ring does not appear in the projection image, but it is clearly seen in the cross-section images.

## 4 Discussion

In the past 20 years, the spatial resolution of fluorescence microscopy has dramatically improved and it is now possible to achieve the resolution below 10 nm using several optical techniques[22]. Despite the development of those super-resolution microscopes and other recent techniques, achieving high spatial and temporal resolution at the same time is still challenging. Cutting-the-edge imaging flow cytometers can record the 3-D image of a stationary/fixed specimen at the imaging throughput of about 50 cells/sec and at the diffraction-limited spatial resolution[23, 24]. Importantly, the existing 3-D methods relying on a scanning mechanism cannot be applied to the specimens that are continuously moving/crawling on a surface or continuously flowing in a channel. 2-D imaging flow cytometers have been commercialized and the list of applications is quickly growing, whereas 3-D imaging flow cytometers have been demonstrated only in a laboratory setting[25, 26]. Several promising techniques have been proposed for snapshot 3-D fluorescence imaging without a scanning mechanism.

In this work, we reported a new technique for 3-D snapshot fluorescence imaging. The technique we named as SPOT uses an MLA as a tube lens to acquire all the projection images in a single snapshot. Extending a theoretical model for high-NA telecentric system, we have developed a forward imaging model for SPOT, which showed that, for a square aperture of size  $p$ , the 2-D point spread function has the FWHM of  $0.443\lambda/\text{NA}_{\text{MLA}}$ . It also showed that each lenslet records a projection image for a different viewing angle, which is determined by the offset of lenslet center and the focal length of OL. We have reconstructed the 3-D fluorescent bead by applying the inverse Radon transform to the projection images. The horizontal and vertical cross-sections clearly showed the optical-sectioning capability of SPOT. We note that the forward imaging model developed in this study can also be used to improve the resolution and accuracy of reconstruction in an iterative reconstruction framework incorporating various *a priori* constraints[27].

As with LFM and other snapshot 3-D imaging, SPOT divides the spatial-bandwidth product of camera to record the sample's depth information, which

typically compromises the field of view, spatial resolution or angular resolution. This problem can be greatly alleviated using a high-resolution camera and an iterative reconstruction incorporating *a priori* information of the sample. Using a high-resolution camera, the imaging throughput may be compromised, which is ultimately limited by the camera frame rate or the data transfer speed to computer, whichever is slower. Importantly, using a snapshot 3-D technique such as SPOT, the motion artefact can be reduced to a negligible level, because the entire volumetric dataset is acquired within the exposure time on the order of microseconds. This is very important for observing a fast, continuous motion in 3-D such as that of freely moving *C. elegans*[28]. In addition to fluorescence signal, SPOT can be applied to record other luminescence signal such as bioluminescence, electroluminescence, radioluminescence, and phosphorescence[29].

## 5 Funding Information

The Lynde and Harry Bradley Catalyst Program.

## References

- [1] B. R. Masters, “Principles of fluorescence spectroscopy,” *Journal of Biomedical Optics*, vol. 13, no. 2, p. 029901, 2008.
- [2] C. J. R. Sheppard, D. M. Shotton, and C. Sheppard, *Confocal Laser Scanning Microscopy. Microscopy Handbook*. New York: BIOS Scientific Publishers Ltd, 1997.
- [3] P. J. Keller, A. D. Schmidt, J. Wittbrodt, and E. H. Stelzer, “Reconstruction of zebrafish early embryonic development by scanned light sheet microscopy,” *Science*, vol. 322, no. 5904, pp. 1065–1069, 2008.
- [4] P. Sarder and A. Nehorai, “Deconvolution methods for 3-D fluorescence microscopy images,” *IEEE Signal Processing Magazine*, vol. 23, no. 3, pp. 32–45, 2006.
- [5] J. Sharpe, U. Ahlgren, P. Perry, B. Hill, A. Ross, J. Hecksher-Srensen, R. Baldock, and D. Davidson, “Optical projection tomography as a tool for 3d microscopy and gene expression studies,” *Science*, vol. 296, no. 5567, pp. 541–545, 2002.
- [6] A. C. Kak and M. Slaney, *Principles of computerized tomographic imaging*. IEEE press New York, 1988.
- [7] J. Geng, “Structured-light 3d surface imaging: a tutorial,” *Advances in Optics and Photonics*, vol. 3, no. 2, pp. 128–160, 2011.
- [8] D. J. Brady, K. Choi, D. L. Marks, R. Horisaki, and S. Lim, “Compressive Holography,” *Optics Express*, vol. 17,

- no. 15, pp. 13 040–13 049, Jul. 2009. [Online]. Available: <https://www.osapublishing.org/abstract.cfm?uri=oe-17-15-13040>
- [9] L. Gao and L. V. Wang, “A review of snapshot multidimensional optical imaging: measuring photon tags in parallel,” *Phys. Rep.*, vol. 616, pp. 1–37, 2016.
  - [10] A. Sinha, G. Barbastathis, W. Liu, and D. Psaltis, “Imaging using volume holograms,” *Optical Engineering*, vol. 43, no. 9, pp. 1959–1972, 2004.
  - [11] P. M. Blanchard and A. H. Greenaway, “Simultaneous multiplane imaging with a distorted diffraction grating,” *Appl. Opt.*, vol. 38, no. 32, pp. 6692–6699, 1999.
  - [12] C. Maurer, S. Khan, S. Fassel, S. Bernet, and M. Ritsch-Marte, “Depth of field multiplexing in microscopy,” *Opt. Express*, vol. 18, no. 3, pp. 3023–3034, 2010.
  - [13] J. Yu, C. Zhou, W. Jia, J. Ma, A. Hu, J. Wu, and S. Wang, “Distorted Dammann grating,” *Opt. Lett.*, vol. 38, no. 4, pp. 474–476, 2013.
  - [14] M. Levoy, R. Ng, A. Adams, M. Footer, and M. Horowitz, “Light field microscopy,” *ACM Trans. Graph.*, vol. 25, no. 3, pp. 924–934, 2006.
  - [15] E. H. Adelson and J. Y. A. Wang, “Single lens stereo with a plenoptic camera,” *IEEE Trans. Pattern Anal. Mach. Intell.*, no. 2, pp. 99–106, 1992.
  - [16] M. Levoy, Z. Zhang, and I. McDowall, “Recording and controlling the 4d light field in a microscope using microlens arrays,” *J. Microsc.*, vol. 235, no. 2, pp. 144–162, 2009.
  - [17] N. Cohen, S. Yang, A. Andalman, M. Broxton, L. Grosenick, K. Deisseroth, M. Horowitz, and M. Levoy, “Enhancing the performance of the light field microscope using wavefront coding,” *Opt. Express*, vol. 22, no. 20, pp. 24 817–24 839, 2014.
  - [18] R. Prevedel, Y.-G. Yoon, M. Hoffmann, N. Pak, G. Wetzstein, S. Kato, T. Schrödel, R. Raskar, M. Zimmer, and E. S. Boyden, “Simultaneous whole-animal 3d imaging of neuronal activity using light-field microscopy,” *Nat. Methods*, vol. 11, no. 7, pp. 727–730, 2014.
  - [19] N. C. Pegard, H.-Y. Liu, N. Antipa, M. Gerlock, H. Adesnik, and L. Waller, “Compressive light-field microscopy for 3d neural activity recording,” *Optica*, vol. 3, no. 5, pp. 517–524, 2016.
  - [20] M. MartAnez-Corral and B. Javidi, “Fundamentals of 3d imaging and displays: a tutorial on integral imaging, light-field, and plenoptic systems,” *Advances in Optics and Photonics*, vol. 10, no. 3, pp. 512–566, 2018.
  - [21] C. J. R. Sheppard and M. Gu, “Imaging by a high aperture optical system,” *J. Mod. Opt.*, vol. 40, no. 8, pp. 1631–1651, 1993.

- [22] C. Cremer and U. Birk, “Perspectives in super-resolved fluorescence microscopy: What comes next?” *Frontiers in Physics*, vol. 4, p. 11, 2016.
- [23] B.-C. Chen, W. R. Legant, K. Wang, L. Shao, D. E. Milkie, M. W. Davidson, C. Janetopoulos, X. S. Wu, J. A. Hammer, and Z. Liu, “Lattice light-sheet microscopy: imaging molecules to embryos at high spatiotemporal resolution,” *Science*, vol. 346, no. 6208, p. 1257998, 2014.
- [24] H. Choi, D. N. Wadduwage, T. Y. Tu, P. Matsudaira, and P. T. So, “Three-dimensional image cytometer based on widefield structured light microscopy and high-speed remote depth scanning,” *Cytometry Part A*, vol. 87, no. 1, pp. 49–60, 2015.
- [25] J. Wu, J. Li, and R. K. Chan, “A light sheet based high throughput 3d-imaging flow cytometer for phytoplankton analysis,” *Opt. Express*, vol. 21, no. 12, pp. 14474–14480, 2013.
- [26] Y. Sung, N. Lue, B. Hamza, J. Martel, D. Irimia, R. R. Dasari, W. Choi, Z. Yaqoob, and P. So, “Three-dimensional holographic refractive-index measurement of continuously flowing cells in a microfluidic channel,” *Phys. Rev. Appl.*, vol. 1, no. 1, p. 014002, 2014.
- [27] T. Blumensath and M. E. Davies, “Iterative hard thresholding for compressed sensing,” *Appl. Comput. Harmon. Anal.*, vol. 27, no. 3, pp. 265–274, 2009.
- [28] M. Shaw, H. Zhan, M. Elmi, V. Pawar, C. Essmann, and M. A. Srinivasan, “Three-dimensional behavioural phenotyping of freely moving *C. elegans* using quantitative light field microscopy,” *PLoS One*, vol. 13, no. 7, p. e0200108, 2018.
- [29] C. R. Ronda, *Luminescence: from theory to applications*. John Wiley & Sons, 2007.